A Model for Nucleation When Nuclei Are Nonstoichiometric: Understanding the Precipitation of Iron Oxyhydroxide Nanoparticles

Benjamin A. Legg[‡,†], Mengqiang Zhu[‡], Hengzhong Zhang[†], Glenn Waychunas[‡], Benjamin Gilbert[‡], and Jillian F. Banfield[†]

[†] Earth and Planetary Science, University of California-Berkeley, Berkeley, California 94720, United States

[‡] Energy Geosciences Division, Lawrence Berkeley National Laboratory, Berkeley, California 94720, United States

Publication Date (Web): August 25, 2016

DOI: 10.1021/acs.cgd.6b00809

Synopsis

We present a variation of classical nucleation theory that can account for surface adsorption, which may facilitate nucleation by reducing the surface tension of the nucleus. We apply this to understand FeOOH nucleation from $FeCl_3$ solutions. Our results suggest that coadsorption of H^+ and Cl^- ions reduces surface tension to a point where classical nucleation mechanisms can operate.

Abstract

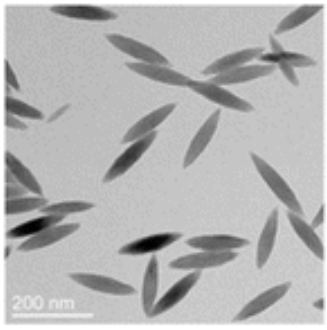

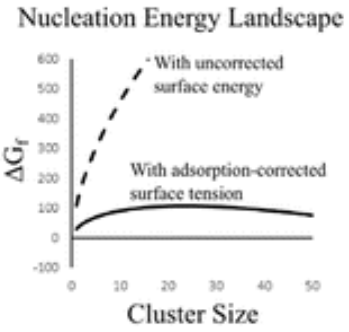

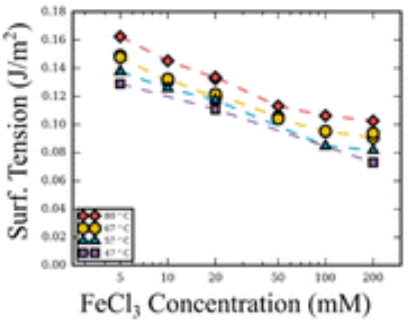

Despite years of study, quantitative models for the nucleation and growth of metal oxyhydroxide nanoparticles from aqueous solution have remained elusive. The problem is complicated by surface adsorption, which causes the stoichiometry of the nucleus to differ from that of the bulk precipitate and causes the surface tension of the precipitate-water interface to depend upon solution chemistry. Here we present a variation of classical nucleation theory that can accommodate surface adsorption, and apply it to understand the nucleation of β-FeOOH (akaganeite) nanoparticles from aqueous $FeCl_3$ solutions. We use small-angle X-ray scattering (SAXS) to quantify nucleation rates over a range of concentrations (5–200 mM $FeCl_3$) and temperatures (47–80 °C), then apply our model to estimate the critical nucleus size and surface tension at each condition. The surface tension varies from 0.07 J/m^2 in 200 mM solutions to 0.16 J/m^2 in 5 mM solutions. This behavior indicates that the nuclei contain an excess of Cl^- and H^+relative to the ideal FeOOH stoichiometry, and the coadsorption of Cl^- and H^+ is critical for reducing surface tension into a range where classical nucleation pathways can operate. Furthermore, we find that the surface tension can be roughly estimated from aqueous solubility data alone, which may help to understand systems where surface tension data is unavailable.

Introduction

Nucleation and growth are topics of broad scientific and engineering importance. Classical nucleation theory (CNT) is commonly used to model the rate of particle formation during mineral precipitation, materials synthesis, and nanoparticle generation.(1-4) When paired with an appropriate model for particle growth, it is possible to describe the overall precipitation rates and understand the development of particle size distributions. However, it has been challenging to apply CNT to many systems. This has been especially true for the precipitation of metal oxyhydroxides from aqueous solution.

According to classical nucleation theory, an energy barrier to particle formation arises due to the work of generating new interfaces. The surface tension of precipitate–water interface thus plays a crucial role in determining the nucleation rate. In fact, the nucleation rate is so sensitive to small changes in surface tension that measurements of nucleation rate have historically provided the best known estimates for the surface tension of many minerals, as demonstrated by the work of Nielson and Söhnel.(5) The sensitivities are such that if the driving force for precipitation (i.e., the solution saturation) is known, only rough proxies for the nucleation rate (such as the induction time needed to see visible precipitates) have proven adequate to estimate the surface tensions in many minerals.(5-7)

To date, we are aware of no studies that have successfully used experimental nucleation rates to estimate the surface tension of iron oxides. This may be due to several complexities involved in iron oxide precipitation. First, ferric iron displays a complex solution chemistry involving multiple hydrolysis states and small polymeric species(8-10) that must be accounted for in order to determine the driving force for precipitation. Second, the rate of nucleation can be difficult to measure because the precipitation of iron oxides is often a multistep process that involves multiple phase transformations,(11-13, 48) and subsequent crystal growth may involve a competition between classical molecule-by-molecule growth and nonclassical aggregation mediated processes(14, 15) that can obscure the nucleation rate.

Perhaps the most important phenomena that must be accounted for when modeling the nucleation and growth of iron oxides is the fact that the stoichiometry of nuclei may deviate from that of the ideal precipitate. It is well-known that iron oxide surfaces in electrolyte solutions may become protonated at low pH. As a result of this surface protonation, the small clusters involved in nucleation may possess an excess of protons relative to a similar quantity of the bulk precipitate. According to the Gibbs adsorption theory, this surface adsorption effect must cause the surface tension of protonated clusters to vary systematically with changes in pH and also cause the surface tension to differ systematically from the “surface excess free energy”. Thus, the current best known values for iron oxyhydroxide interfacial energies (such as those based on calorimetric measurements of the interfacial enthalpy, as reported in refs 12 and 16) cannot be directly applied to model nucleation in low pH solutions without an appropriate correction.

In this study, we have identified a model system where the problem of iron oxyhydroxide nucleation is tractable: the batch precipitation of β-FeOOH nanoparticles via thermal hydrolysis of aqueous $FeCl_3$ solutions. This system is ideal for exploring nucleation and growth because it is a well-studied system that produces particles with well-defined phase, size, and shape, with limited particle aggregation during the course of precipitation.(17-22) Furthermore, the aqueous speciation of small iron complexes in ferric chloride solutions has been studied in detail by Liu and Millero,(9) and others,(23) so that the thermodynamic parameters that are needed to estimate solution saturation are well-known.

In this study, we obtain quantitative descriptions of precipitation using small-angle X-ray scattering (SAXS), which has proven to be a powerful tool for providing time-resolved characterization of nanoparticle precipitation processes.(24-29) In recent years, it has been applied to study the nucleation of iron oxyhydroxide phases.(30, 31) By providing a time-resolved measurements of the total mass precipitated and the average particle size, SAXS allows us to estimate the rate of nanoparticle nucleation over a wide range of experimental conditions.

Having obtained quantitative estimates for the nanoparticle nucleation rates, we then follow the approach of Nielson and Söhnel(5) and apply CNT to determine the surface tension. However, we make several modifications to their approach: (1) we have applied chemical equilibrium calculations to account for the chemical speciation of small iron clusters; (2) we use a model for the nucleus that allows for nonstoichiometric nuclei (i.e., surface adsorption); (3) we use experimentally obtained growth-rate data to estimate the kinetics of molecular attachment; and (4) we develop a self-consistent formulation of CNT that enables us to describe the smallest molecular-scale clusters within the same energetic framework that we use to treat larger nuclei. With our nucleation model, we are able to estimate the size of the nucleation barrier at each experimental condition and determine how the surface tension varies with solution chemistry.

As we will demonstrate, the concentration-dependence of the nucleus surface tension can also provide useful insights into the properties of the nucleus. Through application of the Gibbs adsorption equation, it is possible to estimate the excess quantities of H^+ and Cl^- that are associated with the surface of the nucleus. In this way, we can estimate not only the size of the nucleus, but also its stoichiometry.

Theory

Our analysis is based upon a simple variation of the Becker-Döring classical nucleation theory. Akaganeite nanoparticles are assumed to nucleate from small clusters of atoms that occur naturally in solution due to statistical fluctuations. Becker-Döring theory classifies these clusters by a size index, n. For this system we chose to classify clusters by the number of iron atoms they contain. Each cluster size will possess a free energy of formation, ΔG_n, which can be used to predict the number of clusters in solution, N_n, according to the Boltzmann-type Volmer–Weber distribution.

$$N_n = N_0 \cdot \exp\left(-\frac{\Delta G_n}{k_b T}\right) \quad (1)$$

This expression strictly applies only to cluster distributions within equilibrium solutions, but it should be approximately correct in nonequilibrium solutions for small clusters (clusters that are much smaller than the critical nucleus size). Following the classical approach, we assume that the free energy of cluster formation can be approximated by decomposing it into a volume scaling term and a surface scaling term as follows:

$$\Delta G_n = -nk_b T\sigma + \alpha n^{2/3}\gamma \quad (2)$$

The first term, $-nk_bT\sigma$, represents the free energy change to the system if n formula units of the ideal β-FeOOH solid were precipitated from solution. This driving force is written in terms of the solution saturation parameter, σ, which in turn depends on the chemical activity of small molecular species in solution and the β-FeOOH solubility product. In this system, $\sigma = \ln(\{Fe^{3+}\}/$

$\{H^+\}^3$) – ln(K_s). The second term in eq 2 is an energetic correction term associated with the finite cluster size, and is primarily due to the presence of an interface. The factor $\alpha n^{2/3}$ represents the surface area of the cluster and γ is the surface tension of the cluster–water interface.

Within the literature, many subtle variations of both eq 1 and eq 2 can be found. However, it is important that we use a formulation of CNT that is *self-consistent*, by which we mean that eq 1and eq 2 can predict the equilibrium cluster population across scales, even for the smallest molecular clusters and monomers. This is especially important for modeling iron oxyhydroxide nucleation, since we will show that the nuclei themselves can be very small. It may initially seem strange to describe small molecules and monomers as "clusters" that possess a surface area, but we consider this the most intuitively simple approach. There is no clear cutoff size where molecules transition to particles. Thus, we take inspiration from Einstein, who derived his theory of Brownian motion on the insight that small molecules must be subject to the same thermodynamic laws as particles.(34) However, not all formulations of CNT display this type of self-consistency. In order to obtain a self-consistent description of small clusters, it was important that we adopted a "site-normalized" formulation of CNT, where N_0 is taken to represent the number of *sites* where nucleation can occur (N_0 ≈ 55.7 mol/L for aqueous systems). In contrast, many studies utilize "solute-normalized" formulations of CNT, where N_0 would be taken to represent the number of iron monomers. Although commonly used, solute-normalized formulations of CNT have been shown to produce thermodynamically inconsistent descriptions of small clusters unless significant modifications are made to the functional form eq 2.(35)

The surface tension plays an especially important role in eq 2. First, note that we refer to γ as the *surface tension*, rather than *surface excess energy*. These terms have distinct thermodynamic definitions within the literature on surface adsorption (see ref 33), and surface tension is appropriate here (see Supporting Information Section 3.4). In order for eq 2 to be exactly correct, it is necessary that γ will vary with cluster size. However, it is typical in nucleation theory to assume that these variations are small and treat γ as a constant. This is known as the capillarity approximation, and we adopt it in this study. One cannot know how reliable this approximation is a priori, but we will demonstrate later that it provides a reasonably good description of this system. We will do this by comparing the energetic properties of larger nuclei with the known energetic properties of very small molecular clusters.

The method we use to define a cluster's size and surface area is directly analogous to the method Gibbs prescribed for placing a dividing surface. We define the cluster's size and surface area to be a function of n (the cluster size) by treating cluster as a sphere with a volume of nv, where v is the unit volume of the bulk precipitate, with v = 41.0 Å^3 for β-FeOOH. Using a spherical reference geometry, $\alpha = (36\pi v^2)^{1/3}$. This approach provides an unambiguous definition for the volume and surface area of small clusters and iron monomers, even when the precise structure of these clusters is unknown. This approach enables the development of a self-consistent nucleation theory, and it also makes intuitive sense. It would be much stranger to assign small molecules a surface area of zero, when their formation acts to maximize the amount of interface between solute and solvent. Another advantage of defining volume in terms of iron content is that it defines clusters whose "surface excess quantities" of Fe^{3+} are near zero (i.e., $\Gamma_{Fe^{3+}} \approx 0$). This condition of "equimolarity" with respect to iron allows the surface tension to be independent of Fe^{3+} activity, as discussed by Vehkamäki.(32) (Depending on how iron content is determined, some minor

deviations from Fe^{3+} equimolarity may arise. For more information on calculating surface excess quantities, see ref 33 or Supporting Information Section 3.4.)

Returning to the standard derivation of classical nucleation theory, we now consider the energy landscape for nucleation. In supersaturated $FeCl_3$ solutions, both the saturation parameter σ and γ are positive. Application of eq 2 then predicts that the free energy of cluster formation will display a maximum of ΔG^* at some critical size of n^*. The properties of this critically sized cluster can be estimated as follows:

$$\Delta G^* = \frac{16\pi\gamma^3 v^2}{3(k_b T\sigma)^2} \qquad n^* = \frac{32\pi\gamma^3 v^2}{3(k_b T\sigma)^3} \quad (3)$$

The formation of this nucleus represents an activated process for particle nucleation. The Becker-Döring theory shows that the rate of particle nucleation, *I*, will depend sensitively on the properties of this nucleus. This rate is proportional to the concentration of critically sized nuclei; thus, it depends exponentially on ΔG^*. The rate calculation also includes a factor A' that describes the frequency of molecule attachment and detachment to the nucleus, and a factor *Z*, which is known as the Zeldovich factor.

$$I = A'ZN_0 \exp\left(\frac{-\Delta G^*}{k_b T}\right) \quad (4)$$

If we assume that the frequency of molecule attachment scales with the surface area of the critical nucleus, then the growth kinetics can be written in terms of a normalized parameter, *k*, which describes the rate of monomer attachment to a cluster per unit area. For this special case, the Becker-Döring steady state nucleation rate can then be written explicitly as follows (see Supporting Information Section 3.3)

$$I = k2v\left(\frac{\gamma}{k_b T}\right)^{1/2} N_0 \exp\left(-\frac{16\pi\gamma^3 v^2}{3(k_b T)^3\sigma^2}\right) \quad (5)$$

The nucleation rate depends exponentially upon γ^3 and this sensitivity can be exploited to determine γ, as Nielson and Söhnel have demonstrated. Solving eq 5 for γ, we can obtain an analytical expression for γ as a function of the solution saturation, temperature, and nucleation rate. This expression includes the function $W_{-1}(x)$, which is the Lambert *W* function, evaluated on the −1 branch, which can be approximated as $W_{-1}(x) \approx \ln(-x) - \ln(-\ln(-x))$.

$$\gamma = k_b T\left(\frac{\sigma^2}{32\pi v^2} W_{-1}\left(\frac{\pi}{2\sigma^2 v^4}\frac{I^6}{k^6 N_0^6}\right)\right)^{1/3} \quad (6)$$

Experimental Design and Methods

In this experiment, β-FeOOH nanoparticles were generated by thermally induced hydrolysis of $FeCl_3$ aqueous solutions, at concentrations of 5, 10, 20, 50, 100, and 200 mM. Each of these solutions are supersaturated with respect to formation of β-FeOOH. Precipitation was initiated by placing a small sample tube of solution (2-mm-diameter Kapton tube) into a temperature controlled preheated copper block, at temperatures of 47, 57, 62, 67, 73, or 80 °C. The precipitation reaction was

tracked using in situ small-angle X-ray scattering (SAXS) at Lawrence Berkeley National Laboratories, Advanced Light Source, beamline 7.3.3.(36) Data acquisition began approximately 2 min after the sample was place in the heated block. After the experiments, data processing was performed using the Nika and Irena software suite(37) and with custom code derived from standard analytical theories(38, 39) (details in Supporting Information, Sections 1.2–1.7) in order to obtain the average particle size, total precipitated volume, and estimated number of particles. At the conclusion of each experiment, samples were removed from the copper sample holder and cooled to room temperature. Selected transmission electron microscopy (TEM) samples were then prepared to document particle size, shape (aspect ratio), and crystal structure.

Results

Aqueous Speciation

The variety of conditions probed allows us to sample a range of both initial solution saturations and temperatures. The saturation parameter for precipitation of β-FeOOH is defined as $\sigma = \ln(\{Fe^{3+}\}/\{H^{+}\}^{3}) - \ln(K_s)$, where K_s is the equilibrium solubility product of β-FeOOH. This expression does not directly account for the structural incorporation of Cl^-, which can be found in variable quantities within the β-FeOOH tunnel structure.(40) Therefore, any Cl^- incorporation into the nucleus will be treated as a surface adsorption phenomena. We utilize Visual MINTEQ 3.0 aqueous speciation calculations in order to estimate the activities of $\{Fe^{3+}\}$ and $\{H^{+}\}$ in the initial solutions, and also to calculate how these values evolve during the course of the reaction. The thermodynamic stabilities of solution species in these calculations were taken from the work of Liu and Millero, (9) and Martell,(23) and ionic strength activity corrections were performed using the Davies equation.

The solubility of β-FeOOH is expected to be slightly larger that of goethite, but smaller than that of ferrihydrite.(41) Based upon the work of Mazeina et al.,(16) the solubility is expected to have a value of $K_s = 10^{2.0}$ at 25 °C, but because the enthalpy of dissolution is −65.4 kJ/mol (exothermic dissolution), the solubility decreases with increasing temperature. In this study, we assumed the same temperature dependence as Mazeina et al., but used complementary experiments to obtain a revised value for the solubility at 25 °C. We prepared 5 mL samples of $FeCl_3$ solutions (concentrations from 5 mM to 800 mM) in sealed glass vials, placed them in an oven for 24 h at 80 °C, and allowed them precipitate to reach equilibrium. The supernatant solution was obtained by filtering with a 0.1 μm Supor filter, and the supernatant iron concentration was measured by 600 nm UV–vis adsorption with a ferron assay,(42) and solution pH was measured with Ag–AgCl electrode. Comparison of the supernatant iron concentration with MINTEQ models suggest that β-FeOOH has a solubility constant of $K_s = 10^{2.3}$ at 25 °C, which is in good agreement with expectations. (See Section S1.8 for more details.)

Two atypical behaviors of $FeCl_3$ solutions should be noted. First, for concentrations below ∼150 mM, the initial supersaturation with respect to β-FeOOH decreases as the $FeCl_3$ concentrations are increased. This is related to the acid–base chemistry of $FeCl_3$ solutions; for $FeCl_3$concentrations below 150 mM the pH of solution drops with increasing concentration. Second, β-FeOOH dissolution is an exothermic process, which leads to a saturation that increases with temperature. Figure 4 includes a contour plot of the initial supersaturation, σ_{init}, over the range of temperatures and concentrations tested.

TEM Observations

TEM observations show that particle size and shape change systematically with the conditions of precipitation. When $FeCl_3$ concentrations are low, the solution supersataturation is relatively high (as discussed above), and very small particles are observed, as shown in Figure 1A. However, at concentrations near 100 mM, solution supersaturations are lower and much larger particles are observed, as shown in Figure 1B. The increased particle size indicates that nucleation rates have decreased relative to growth rates. Particle aspect ratio also varies with concentration, with higher concentrations generally producing more elongated particles. The particle size and aspect ratios for all TEM samples are summarized in Table 1. TEM samples were also obtained for 400 mM samples, but these particles were very elongated and were prone to aggregation, both factors making SAXS analysis difficult. Thus, our detailed nucleation analysis was limited to concentrations of 200 mM or less.

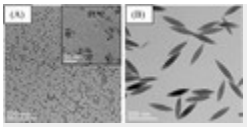

Figure 1. TEM images of nanoparticles precipitated at (A) 5 mM $FeCl_3$, 47 °C; (B) 100 mM $FeCl_3$, 57 °C.

Table 1. Summary of Particle Size (Mass-Averaged Radius of Gyration, *r*), and Aspect Ratio (AR), Obtained by TEM Particle Measurement at the Conclusion of SAXS Experiments[a]

		47 °C	57 °C	67 °C	80 °C
5 mM	*r* (nm)	4.0	2.6		
	AR	1.4	1.2		
10 mM	*r* (nm)		4.2		2.9
	AR		1.7		1.4
20 mM	*r* (nm)	44	27	7.0	4.8
	AR	2.9	2.6	2.6	2.0
50 mM	*r* (nm)		107	118	5.9
	AR		3.5	3.4	2.1
100 mM	*r* (nm)		43	47	49
	AR		4.3	4.8	3.6
200 mM	*r* (nm)			23	60

		47 °C	57 °C	67 °C	80 °C
				5.2	4.3
400 mM	*r* (nm) AR			33	
				9.9	

[a] In general, larger particles were obtained from experiments with lower initial supersaturations, and aspect ratios increase with $FeCl_3$ concentration.

High-resolution TEM images with lattice fringe imaging (Figure 2) shows that particles consist of β-FeOOH (akaganeite, space group *I*2/*m*). In general, the particles appear to be faceted, with elongation along the [010] axis. Some degree of crystallographic twinning is observed, consistent with the early observations of MacKay.(43) The precise mechanism of twinning is unknown, although recent work by Asenath-Smith and Estroff(44) has demonstrated that solution pH plays an important role. Particle aggregation appears limited in most samples, but for the 100 mM, 200 mM, and 400 mM samples, the crystals aggregate into rafts and extended 2-D colloidal crystals at later time-points, with an example shown in Figure 2B. Although interesting, this behavior prevents the acquisition of SAXS particle size and number estimates during the later stages of precipitation. First, because the organization into large aggregates would necessitate a more sophisticated SAXS analytical approach than we have used, and second, because aggregation induces particle settling.

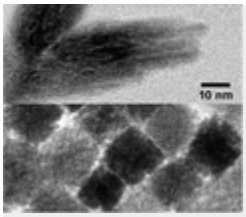

Figure 2. High-resolution TEM images, both obtained at 150k × magnification. Top: side view of a twinned particle synthesized from 100 mM $FeCl_3$ at 67 °C. Prominent (101) fringes are visible. Bottom: Particles synthesized from 200 mM $FeCl_3$ at 67 °C, packed into a 2-D colloidal crystal. Particles are viewed down the [010] (long) axis, and the square cross section terminated by the (100) and (001) faces is visible. The (101) and $(10\bar{1})$ lattice fringes can be seen.

SAXS Precipitation Curves

Figure 3 shows two representative time series of SAXS scattering profiles for precipitation from 5 mM, and 100 mM $FeCl_3$ solutions at 67 °C. Each curve represents a single time point, with measurements taken at 10 s intervals. Over time, the total scattering intensity increases, reflecting an increase in precipitated volume, and there is a general shift toward scattering at smaller angles (lower *q*-values), which reflects increasing particle size. Several higher-order scattering lobes are visible in the 100 mM sample. These indicate that the particles have a well-defined shape and narrow size distribution. The scattering profile of the 5 mM sample extends to higher *q*-ranges, indicating a smaller average particle size. A lack of visible higher-order oscillations in this sample indicates that the particle size and shape in these samples have more variation, and this interpretation is consistent with the TEM images.

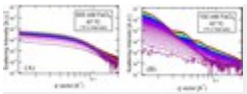

Figure 3. SAXS scattering profiles of nanoparticle precipitation: from (A) 5 mM $FeCl_3$ and (B) 100 mM $FeCl_3$. Both data sets are obtained at 67 °C. Each curve corresponds to one time point, obtained at 10 s intervals.

Particle Nucleation

SAXS data was used to estimate the total number of particles as a function of time for each experiment. We determine total mass precipitated using the Porod invariant method, and average particle volume using the Porod volume, as described in the Supporting Information Section 1.6. The number of particles is then estimated by dividing the total precipitated volume by the average particle volume. Although such approaches are susceptible to systematic error when treating polydisperse particle suspensions, we have estimated that the degree of error is well within our requirements for estimating the nucleation rate (see Supporting Information Section 1.7). Model-based least-squares iterative SAXS fitting approaches were also considered for determining $N(t)$, but these methods were found to be inferior because they are prone to convergence on unphysical values. Such difficulties are commonly encountered with model based approaches, which can have difficulty distinguishing changes in particle shape from variability in particle size.

In general, the rate of particle formation is high at the onset of the experiment, and gradually slows as the experiment progresses. Each experiment was fit to a function of the form $N(t) = N_{max}(1 - \exp(-t/t_{nuc}))$, in order to estimate a time scale for nucleation, t_{nuc}, and the number of particles formed, N_{max}. The initial nucleation rate can subsequently be estimated as $I_{init} \approx N_{max}/t_{nuc}$. These fitting results are provided in Figure 4 and Table 2, with further discussions provided in the Supporting Information.

Table 2. Final Particle Density, N_{max}, the Time Scale of Nucleation, t_{nuc}, and the Initial Nucleation Rate, I_{init}, Are Estimated by Fitting SAXS Particle-Number Data[a]

		47 °C	57 °C	62 °C	67 °C	73 °C	80 °C
5 mM	N_{max} (m^{-3})	6.6×10^{19}	3.2×10^{20}		5.9×10^{20}		9.8×10^{20}
	t_{nuc} (s)	600	240		130		60
	I_{init} ($m^{-3}\ s^{-1}$)	1.1×10^{17}	1.3×10^{18}		4.6×10^{18}		2.3×10^{19}
	σ_{init}	5.4	5.7		6.1		5.3
	k_{init} ($m^{-2}\ s^{-1}$)	2.5×10^{17}	1.4×10^{18}		7.4×10^{18}		5.4×10^{19}
	γ_{init} (J/m^2)	0.129	0.138		0.149		0.162
10 mM	N_{max} (m^{-3})		1.1×10^{20}		4.8×10^{20}		8.8×10^{20}

		47 °C	57 °C	62 °C	67 °C	73 °C	80 °C
	t_{nuc} (s)		350		60		40
	I_{init} (m^{-3} s^{-1})		3.2×10^{17}		8.2×10^{18}		1.8×10^{19}
	σ_{init}		4.9		5.3		5.7
	k_{init} (m^{-2} s^{-1})		6.6×10^{17}		2.5×10^{18}		1.3×10^{19}
	γ_{init} (J/m^2)		0.126		0.131		1.45
20 mM	N_{max} (m^{-3})	3.1×10^{17}	-	8.3×10^{19}	1.4×10^{20}	2.0×10^{20}	2.7×10^{20}
	t_{nuc} (s)	5600	-	430	170	150	100
	I_{init} (m^{-3} s^{-1})	5.7×10^{13}	2.5×10^{15}	1.9×10^{17}	1.2×10^{18}	1.4×10^{18}	3.0×10^{18}
	σ_{init}	3.8	4.1	4.2	4.4	4.6	4.7
	k_{init} (m^{-2} s^{-1})	1.7×10^{17}	7.9×10^{17}	1.7×10^{18}	3.4×10^{18}	7.9×10^{18}	2.1×10^{19}
	γ_{init} (J/m^2)	0.111	0.117	0.117	0.120	0.126	0.133
50 mM	N_{max} (m^{-3})				4.9×10^{18}		7.8×10^{19}
	t_{nuc} (s)				580		120
	I_{init} (m^{-3} s^{-1})				9.8×10^{15}		6.3×10^{17}
	σ_{init}				3.3		3.6
	k_{init} (m^{-2} s^{-1})				2.3×10^{18}		2.0×10^{19}
	γ_{init} (J/m^2)				0.105		0.113
100 mM	N_{max} (m^{-3})		1.8×10^{18}		6.4×10^{17}		2.2×10^{18}
	t_{nuc} (s)		5600		1100		280

		47 °C	57 °C	62 °C	67 °C	73 °C	80 °C
	I_{init} (m^{-3} s^{-1})		3.3×10^{14}		6.1×10^{14}		8.0×10^{15}
	σ_{init}		2.5		2.8		3.1
	k_{init} (m^{-2} s^{-1})		9.9×10^{16}		8.9×10^{17}		1.3×10^{19}
	γ_{init} (J/m^2)		0.085		0.095		0.106
200 mM	N_{max} (m^{-3})		1.7×10^{19}	1.2×10^{19}	9.4×10^{18}	1.6×10^{19}	4.7×10^{18}
	t_{nuc} (s)		2300	900	2000	480	130
	I_{init} (m^{-3} s^{-1})	1.4×10^{15}	7.2×10^{15}	1.4×10^{16}	9.7×10^{15}	2.3×10^{16}	3.5×10^{16}
	σ_{init}	2.2	2.5	2.7	2.8	2.9	3.1
	k_{init} (m^{-2} s^{-1})	1.5×10^{16}	7.4×10^{16}	1.6×10^{17}	3.2×10^{17}	7.6×10^{17}	2.0×10^{18}
	γ_{init} (J/m^2)	0.073	0.081	0.086	0.091	0.096	0.103

[a] The initial supersaturation σ_{init}, is calculated using MINTEQ. The frequency of molecular attachment at the onset of the experiment, k_{init}, is estimated from SAXS growth rate data. The surface tension at the onset of the experiment, γ_{init}, is calculated from these values using eq 6. When multiple experiments were performed at the same condition, an average value is given. Values for each individual experiment are provided in the Supporting Information.

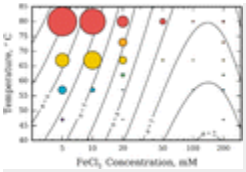

Figure 4. Each bubble represents an experimental condition. The location of the bubble indicates the temperature and concentration at which the experiment(s) were performed. Bubble area is proportional to the estimated initial nucleation rate (average value is used when more than one experiment was performed). The experimental results are superimposed upon a contour plot of the initial solution supersaturation with respect to β-FeOOH, as calculated using MINTEQ, assuming $\log(K_s) = 2.3$ at 25 °C, and dissolution a enthalpy of −65.4 kJ/mol. Although higher supersaturation generally leads to greater nucleation rates, the correlation is not exact due to variations in temperature, attachment kinetics, and surface tension.

The initial nucleation rates vary by 6 orders of magnitude over the range of conditions studied. Nucleation is most rapid in the highly supersaturated 5 mM solutions, and lowest at concentrations near 100 mM. As expected, the nucleation rate shows a strong correlation with the initial supersaturation. However, the correspondence is not exact, which demonstrates the importance of accounting for the influence of temperature, attachment kinetics, and surface tension on nucleation rates.

Particle Growth Kinetics

Although the primary goal of this experiment is to characterize the nucleation process, growth rate data is also analyzed, insofar as it relates to the frequency of molecular attachment, k.

We obtain a rough measure for the growth rate throughout the course of the experiment by tracking the time-derivative of the radius of gyration, $\dot{r}$. The radius of gyration is calculated using the traditional Guinier approximation. This approach is subject to systematic error (primarily associated with particle size dispersity), but a sensitivity analysis suggests that this error is minor. We prefer this approach over iterative SAXS fitting methods, which produce errors that are less predictable. In each experiment, we have determined $\dot{r}$ as a function of the "degree of reaction", x. We have defined x in terms of the precipitated volume fraction, ϕ, as $x = \phi/\phi_{eq}$, such that it has a value of 0 at the onset of the experiment and 1 when equilibrium is reached. In all cases, the growth rates show an approximately exponential decay with respect to x, and a strong Arrhenius-type temperature dependence. There is no strong evidence for particle size effects on the growth rate. For each concentration, we have utilized a least-squares fitting approach to determine an empirical rate law for growth rates, following the functional form of eq 7. We have refrained from using more sophisticated growth models since we do not wish to imply a growth mechanism where none is known.

$$\dot{r}(x) = \dot{r}_0 \exp(-C \cdot x) \exp(E_a/RT) \quad (7)$$

Examples of the growth rate data and corresponding fits are plotted in Figure 5 for solutions at 10 mM and 200 mM $FeCl_3$ concentration. The fitting parameters for all concentrations summarized in Table 3. In all cases, the apparent activation energies for growth, E_a, are very large, in the range of 120 and 200 kJ/mol. However, we cannot reliably identify trends in the activation energy, due to a high degree of correlation between $\dot{r}_0$, and E_a. Nevertheless, the apparent activation energies are quite high: roughly 1 order of magnitude greater than that for molecular diffusion in water, and several times greater than the typical activation energies for olation or oxolation reactions,(7)which suggests that incorporation of new molecules onto the particle surface occurs by a complex, coordinated process.

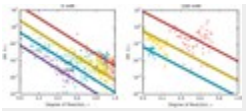

Figure 5. Growth rate, plotted as a function of degree of reaction for two different concentrations. Crosses indicate distinct experimental measurements of the growth rate, while solid lines are fits to the data. Colors indicate the temperature of reaction. Red: 80 °C, Orange: 73 °C, Yellow: 67 °C, green: 62 °C, cyan: 57 °C, purple: 47 °C. Higher temperatures produce faster growth rates.

Table 3. Growth Rate Parameter Fits

[$FeCl_3$], mM	$\dot{r}_0$, m/s	E_a, kJ/mol	C
5	7.5×10^{23}	153	8.3
10	1.2×10^{19}	125	6.9

$[FeCl_3]$, mM	$\dot{r}_0$, m/s	E_a, kJ/mol	C
20	1.3×10^{21}	136	8.2
50	1.6×10^{25}	164	7.5
100	2.0×10^{31}	205	6.9
200	3.8×10^{20}	138	9.3

The initial growth rate cannot be directly measured at all experimental conditions, thus we estimate the initial growth rate by evaluating $\dot{r}(x = 0)$ for each experimental condition, using the values provided in Table 3. The growth rate is converted into a frequency of molecular attachment using simple geometric relations, as described in the Supporting Information Section 3.3. The use of nanoparticle growth rates to estimate k is based upon major two assumptions. First, we are assuming that the frequency of attachment to the advancing surface is much greater than the frequency of detachment, so that growth rates and attachment rates can be directly related. This assumption is likely to be valid due to the high supersaturations being considered. Second, we are assuming that the kinetics of attachment to large particles is a reasonable proxy for the kinetics of attachment to a nucleus. This assumption is justified within limits. Casey, Swaddle, and Rustad(46, 47) have studied the reaction kinetics of small metal oxide clusters, and shown that the reactivity of such clusters may be quite sensitive to small changes in cluster structure or protonation state,(49) but in general they have found that the reactivity of small clusters scales in proportion to the kinetics of dissolution and growth for corresponding macroscopic minerals.

Surface Tension

Having obtained an estimate for σ_{init}, I_{init}, and k_{init}, as described above, we utilize eq 6 to determine a value for the initial surface tension, γ_{init}. The input values and results are reported in Table 2, and the best estimates for γ_{init} are plotted in Figure 6A. The estimated magnitudes of the surface tensions range between 0.06 and 0.14 J/m^2. Two major trends are observed. First, the surface tension decreases systematically with increasing $FeCl_3$ concentration (i.e., lower pH and higher Cl^- concentration). Second, the surface tension increases slightly with temperature. These results have thermodynamic implications that will be discussed later.

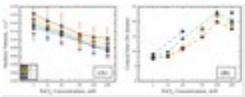

Figure 6. (A) Filled symbols show the surface energies of the critical cluster plotted as a function of the initial $FeCl_3$ concentration, as estimated by modeling precipitation rates. Red diamonds: 80 °C, yellow circles: 67 °C, cyan triangles: 57 °C, purple squares: 47 °C. Open symbols show the surface tension of the monomer species, which was calculated using eq 10, as discussed later in the text. Monomer surface tensions have been plotted at 47 and 80 °C, and although the absolute values are slightly lower than for the critical cluster, the general dependence on temperature and concentration is similar. (B) Estimated number of iron atoms in the critical nucleus at the onset of precipitation, as estimated by modeling precipitation rates. For visual clarity, error bars are omitted in this figure.

Acknowledging that there is a large potential for systematic error in the estimation of k_{init} from growth rate data, and also some potential for error in the estimate of K_s, we have also computed a range of reasonable values for for γ_{init}. We have considered the possibility that k_{init} may reasonably vary from the optimal estimated value by up to 3 orders of magnitude in either direction, and that K_s may also vary by 0.3 units above or below our estimated value. These provide high and low estimates for γ_{init} (reported in the Supporting Information Section 2.3). As can be seen from a sensitivity analysis of eq 6, the nucleation theory is relatively insensitive to such errors, and we find that even in these cases, the high range and low range deviate by less than 10% from the optimal value.

Nucleus Size and Stoichiometry

Having calculated γ_{init}, eq 3 can be applied to estimate other properties of the critical nucleus, such as its free energy of formation and size. The critical free energy of formation at the onset of nucleation (ΔG^*) ranges from 60 to 90 kJ/mol. We also find that the initial nucleus may be extremely small, containing between 5 and 25 iron atoms. The initial nucleus size is plotted in Figure 6B. However, we must recall that both the free energy of formation and the nucleus size will increase as precipitation proceeds and the solution saturation drops.

The systematic trends of solution tension vs concentration can provide useful insights into the nucleus stoichiometry. The Gibbs adsorption equation, $d\gamma = \sum_i \Gamma_i d\mu_i$, tells us that if some chemical species (species *i*) is adsorbed on a surface (i.e., the surface excess quantity, Γ_i, is nonzero), then the surface tension will vary systematically with changes in the chemical potential of that species ($d\mu_i$). Having defined the nucleus to be equimolar with respect to iron, and assuming that the chemical potential of H_2O is nearly independent of $FeCl_3$ concentration, we need only consider surface excess quantities of Cl^- and H^+. Furthermore, these values must be equal in order to maintain long-range charge balance (i.e., $\Gamma_{Cl^-} = \Gamma_{H^+}$). The derivative of γ with respect to $RT(\ln\{Cl^-\} + \ln\{H^+\})$ will thus provide an estimate of the surface excess concentration. In Figure 7, we find that this derivative is roughly independent of temperature, and it corresponds to surface excess quantities of $\Gamma_{Cl^-} = \Gamma_{H^+} \approx 2.4 \pm 0.2/nm^2$. (Note that these quantities do not distinguish between specifically adsorbed ions and those in the diffuse swarm.) Our results are not sufficiently accurate to distinguish how the surface excess quantities change in response to solution chemistry. We would expect that surface excess quantities of Cl^- and H^+ will increase as the $FeCl_3$ concentration is raised, and hence the slope in Figure 7 should become more negative toward the left, but this behavior is not seen. However, our results can be compared with titration measurements on bulk akaganeite by Kanungo,(50) who measured quantities of adsorbed H^+ at pH 3.5 ranging from 1.2 in 1 mM NaCl to 4.2/nm^2 in 0.5 M NaCl. Our results fall within this range, but direct comparison is obscured because of differences in the material being analyzed (small nuclei vs large particles) and the definitions of surface area (the Kanungo study determines surface area through gas adsorption measurements). Furthermore, as Kozin and Boily(51) noted, there is a need to distinguish between bulk incorporation and surface adsorption when considering large particles.

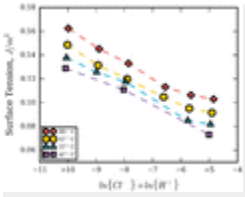

Figure 7. Dependence of surface tension on $\{Cl^-\}$ and $\{H^+\}$ is an indication of the surface excess quantities of these species. The slope of this plot is indicative of the surface excess concentrations of Cl^- and H^+. These two surface excess quantities are assumed

to be equal to each other, which is necessary to preserve charge balance. For visual clarity, error bars have been omitted, but have been presented for the equivalent data in Figure 6A.

Discussion

Surface Tension

The surface tensions we determine for the critical cluster (between 0.07 and 0.16 J/m^2) are significantly lower than literature values for the excess interfacial enthalpy of hydrated iron β-FeOOH surfaces, which range from 0.34 J/m^2 at 25 °C to 0.44 J/m2 at 70 °C.(12) These values are not necessarily in conflict. Rather, they indicate the importance of distinguishing between surface tension and surface excess energy, and the importance of accounting for changes in surface tension due to adsorption phenomena.

We note that we have estimated γ_{init} for the experiment onset, but γ should vary during the course of an experiment in response to changing pH. This dependence can by predicted by application of the Gibbs adsorption equation if we know the surface stoichiometry (which was estimated above). Although the surface stoichiometry itself may also vary with pH, these stoichiometric variations will only result in second-order corrections to the surface tension.

Because the surface tension appears to increase with temperature, this suggests a significant entropic contribution to the surface tension. Such negative interfacial entropies would be consistent with having structured water at the cluster interface.

Confirmation of Results: Precipitation Modeling

The results above are all contingent upon the assumption that CNT provides a reasonable representation of the precipitation process. Thus, we have taken two distinct approaches to confirm the reasonableness of our assumptions. In the first approach, we recognize that SAXS analysis provides a rich data set which allows us to not only determine the initial nucleation and growth rates, but also track the evolution of particle number, particle size, and total mass precipitated over time. If the classical nucleation and growth models are accurate, it should be possible to qualitatively reproduce the mass-precipitation curve using numerical simulation. We have attempted this by solving the integral equation shown as eq 8, in order to obtain the total mass precipitated as a function of time. This equation is solved numerically, since the complex saturation dependence of both nucleation and growth rates makes an exact analytic solution intractable. The equation assumes a quasi-steady-state model of nucleation, where the nucleation rate at any moment is given by the Becker Döring steady-state nucleation rate, but where this rate evolves over time in response to changing supersaturation, growth kinetics, and surface tension. In comparison, the commonly used Avrami precipitation models must assume much simpler functional forms for the nucleation and growth rates.

$$x(t) = \frac{1}{\phi_{eq}} \int_{t'=t_v}^{t} I(x)\alpha\left(\int_{t''=t'}^{t} \dot{r}(x)\, dt''\right)^3 dt' \quad (8)$$

Simulated precipitate profiles are provided in Supporting Information Section 2.2, where they are compared with experimental results in detail. When interpreting these results, we note that perfect agreement should not be expected. The actual physical phenomena being predicted are very complex, and we are attempting to fit a large range of experimental conditions with just

one physical model and very few adjustable parameters. In this light, we find that the kinetic models do a remarkable job of reproducing the essential characteristics of the experimental data. They produce an appropriate sigmodal shape to the precipitation profile, where precipitation is slow initially due to a lack of surfaces for growth, accelerates as new growth surfaces become available, and later tapers off in response to dropping solution saturation. They also capture essential trends, accurately reflecting how the shape of the precipitation profile responds to changes in temperature and concentration. For example, the period of accelerating precipitation is very brief at high temperatures and low concentrations, but may persist for many minutes or hours when the temperature is lower or the concentration higher. We take this qualitative agreement as confirmation that our CNT based model of precipitation is reasonable.

Monomer Surface Tension and Solubility Relationship

As a second way to confirm the validity of our results, we will compare our results with known energetic properties for small molecular clusters. As discussed before, we have sought to develop a formulation of classical nucleation theory that is self-consistent, so that the free energy of formation for small molecules (even iron monomers) can be described using eq 2. Because the thermodynamic properties of dissolved monomers are well-known, we are able to directly calculate the surface tension of the monomer. Then by determining the surface tension of the monomer with surface tension of the nucleus, we can estimate how much γ varies with cluster size. If the values are close, this will validate our use of the capillarity approximation.

In order to determine the surface tension of the monomer in our self-consistent framework, we combine eq 2 with eq 1 to obtain the following expression:

$$\gamma = \left(nkT\sigma - kT\ln \frac{N_n}{N_{tot}} \right) / an^{2/3} \quad (9)$$

In the case of small molecules, if we are given a solution condition, we can easily use MINTEQ calculates to predict both σ and N_n. For example, the concentration of dissolved iron monomers in a solution can be calculated as N_1/N_{tot} = $[Fe^{3+}]$ + $[Fe(OH)^{2+}]$ + $[FeOH^{2+}]$ + $[Fe(OH)_3]$ + $[Fe(OH)_4^-]$ + $[FeCl^{2+}]$. Since the surface tension is nearly independent of solution saturation state, we may choose to for simplicity to calculate the quantity of dissolved iron monomers in a *saturated* solution of fixed pH and Cl^- activity. This leads to a simpler expression, since σ = 0 in the saturated solution. Thus, we obtain the following simple expression for the surface tension of a monomer (where X_{sat} is the mole fraction of iron monomers in a saturated solution):

$$\gamma_1 = (-kT\ln X_{sat}) / (36\pi v^2)^{1/3} \quad (10)$$

When these monomer surface tensions are plotted alongside the estimated surface tension of the nuclei in Figure 6, remarkably good agreement is seen. The absolute magnitudes are very similar (typically differing by less than 25%), which validates the use of the capillarity approximation (see Supporting Information Sections 3.3–3.5). Furthermore, the trends with respect to temperature, pH, and Cl^- concentration are replicated very well. This supports the concept that iron monomers can be treated as small clusters, and shows us that they share important chemical features with the larger nucleation clusters. We can understand these chemical features better if we recognize our thermodynamic framework for the cluster treats ion complexation as a form of surface adsorption. Here, when the iron monomer is found to have a surface excess of protons relative to FeOOH, it is because “protonated” species such as Fe^{3+}, $Fe(OH)^{2+}$, and $Fe(OH)_2^+$ are far more common in acidic $FeCl_3$ solutions than the neutral $Fe(OH)_3$ species.

The relatively good agreement between the monomer surface tensions calculated from eq 10 and the surface tensions that have been estimated from nucleation rate data raises the possibility that eq 10 could be used to predict the surface tension of other phases. This approach has strong precedent. Grosse has previously shown correlations between the surface energy of a liquid metal and its heat of vaporization,(45) while Nielsen and Söhnel(5) and Mersmann(6) established an empirical relationship between the solubility of ionic solids and their surface tensions. The exponential relationship between solubility and surface tension that we have derived in eq 10 is nearly identical to the relationship found by Nielsen and Söhnel. Obviously we do not expect that eq 10 will provide perfect predictions of cluster surface tensions; significant structural and energetic differences will exist between the monomer–solvent interface and the cluster–solvent interface. We see disagreements on the order of 25% within this data set. Nevertheless, values of X_{sat} for many phases are readily available through the use of programs such as MINTEQ and from books such as Baes and Mesmer.(30) Thus, we expect that eq 10 may serve as an easy way to estimate the pH-dependent surface tension of other oxyhydroxide phases, which may be very useful since direct measurements of surface tension are generally unavailable at this time.

Nature of the Nucleus

At the onset of nucleation, it appears that the critical nuclei are small clusters, with best estimates of size ranging from 5 to 25 Fe atoms, and they possess an excess of protons and chlorine relative to the ideal FeOOH stoichiometry. These clusters are clearly too small to be considered crystalline, and it will be an interesting topic of future work to determine what structural and compositional properties are possessed by members of the critically poised cluster ensemble. Because the early nuclei are so small, computational modeling may soon be able to explore this question in greater detail.

Limits of Classical Nucleation Theory

The small nucleus size indicates that this system operates near the limits of the classical nucleation theory. Having shown that n^* depends on solution chemistry, it interesting to consider how small the critical size can become. As n^* approaches a value of less than two, the primary assumptions which underlie system Becker-Döring nucleation theory can no longer hold; the system will clearly become unstable. A scaling-law analysis can be used to predict when such instabilities will occur. To the first approximation, sizable nucleation rates will only occur if ΔG^* drops below some critical threshold, on the order of 30 or 40 kT. According to eq 3, ΔG^* scales like γ^3/σ^2. Thus, if γ is increased, then σ must also be increased to compensate. However, n^* scales like γ^3/σ^3, so systems with larger γ will tend to have smaller critical nuclei. Indeed, we see this behavior in the nucleation of FeOOH; nucleation at higher pH is involves nuclei with higher surface tension, but smaller size. However, if γ is raised too high (above ∼250 mJ/m^2 in the FeOOH system), then the supersaturations required to bring ΔG^* into a feasible range would drive n^* down below 2. This will cause a solution instability and nucleation will not occur by the Becker-Döring mechanism. When we recognize that surface tension is pH dependent, this may explain the difficulties that have previously been encountered when trying to model nucleation of iron oxyhydroxides at near-neutral conditions (for example, during base-induced hydrolysis of ferric salts). Conversely, the well-controlled nucleation behavior of akaganetite seems to be made possible by the coadsorption of Cl^- and H^+, which reduces the surface tension into a regime where classical nucleation can occur.

Conclusion

In this work, the nucleation and growth of β-FeOOH (akaganeite) nanoparticles were studied using in situ small-angle X-ray scattering (SAXS). This system proves to be an ideal model system to study precipitation, with nucleation rates, growth rates, and particle aspect ratios being systematically tunable by simple variations in $FeCl_3$ concentration and temperature. In order to analyze this system, it was necessary to develop a formulation of classical nucleation theory that can accommodate surface-adsorption phenomena.

Analysis of the measured initial nucleation rates and growth kinetics allows us to determine an estimate of the surface tension of the critical nucleus. This represents the first quantitative determination of an iron oxyhydroxide surface tension under the low pH conditions that are relevant to nanoparticle formation. Our values (0.08–0.16 J/m^2) are found to be significantly lower than commonly used proxies, such as the interfacial enthalpy. The surface tension is dependent on $FeCl_3$ concentration, and we interpret this as a response to changes pH and Cl^- activity, which occurs due to the coadsorption of H^+ and Cl^- onto the nucleus. The surface tension also increases with temperature, which suggests that a negative surface entropy is a significant contribution to the surface tension.

Our finding is that the critical nucleus may be very small, initially containing just 5 to 25 iron atoms. This may present opportunities for future investigation since clusters of this size range can be modeled with modern computational methods. More importantly, this small size suggests that precipitation is occurring near the limits of the classical nucleation regime. We speculate that moderately higher surface tensions and saturations will decrease the nucleus size further, and may even produce conditions where precipitation proceeds by nonclassical pathways. The relatively well controlled precipitation behavior that we have observed for β-FeOOH may in fact be a consequence of Cl^- and H^+ coadsorption serving to reduce the surface tension into a regime where precipitation can occur by classical nucleation.

Furthermore, our thermodynamic treatment of the nucleation clusters was designed to be self-consistent, in the sense that it allows us to define a surface tension for clusters of all sizes, including dissolved monomers. The surface tensions of the monomers can be readily calculated on the basis readily available thermodynamic solubility data, and is found to agree well with the surface tension that we have obtained for larger nucleation clusters. This suggests that solubility data may provide a method for estimating the surface tension of oxyhydroxide phases when better data is not available.

Although this study has focused on the nucleation of FeOOH, there are a large number of oxyhydroxide minerals with geochemical behavior that is similar to FeOOH, but for which detailed nucleation modeling has not yet been performed. Thus, we hope that the methods presented can eventually be adapted to understand a wider range of important systems.

Supporting Information

The Supporting Information is available free of charge on the ACS Publications website at DOI: 10.1021/acs.cgd.6b00809.

The authors declare no competing financial interest.

Acknowledgment

This work was supported by the Director, Office of Science, Office of Basic Energy Sciences, Division of Chemical Sciences, Geosciences, and Biosciences, of the U.S. Department of Energy under Contract No. DE-AC02-05CH11231. We thank Roseann Csencsits of Lawrence Berkeley National Laboratory for support with TEM image acquisition. We thank Alexander Hexemer, Steven A. Alvarez, and Eric Schaible for the support with SAXS data acquisition. SAXS experiments were performed at the Advanced Light Source, a user facility at Lawrence Berkeley National Laboratory supported by the Director, Office of Science, Office of Basic Energy Sciences, of the U.S. Department of Energy under Contract DE-AC02-05CH11231.

References

This article references 51 other publications.

1. Melia, T. P. Crystal Nucleation from Aqueous Solution *J. Appl. Chem.* **1965**, 15, 345– 357 DOI: 10.1002/jctb.5010150801
2. Christian, J. W. *The Theory of Transformations in Metals and Alloys*, 3rd ed.; Pergamon: New York, **2002**; pp 422– 461.
3. Sugimoto, T. Underlying Mechanisms in Size Control of Uniform Nanoparticles *J. Colloid Interface Sci.* **2007**,309, 106– 118 DOI: 10.1016/j.jcis.2007.01.036
4. Mersmann, A. Crystallization and Precipitation *Chem. Eng. Process.* **1999**, 38, 345– 353 DOI: 10.1016/S0255-2701(99)00025-2
5. Nielsen, A. E.; Söhnel, O. Interfacial Tensions Electrolyte Crystal-Aqueous Solution, From Nucleation Data*J. Cryst. Growth* **1971**, 11, 233– 242 DOI: 10.1016/0022-0248(71)90090-X
6. Mersmann, A. Calculation of Interfacial Tensions *J. Cryst. Growth* **1990**, 102, 841– 847 DOI: 10.1016/0022-0248(90)90850-K
7. Jolivet, J. P. *Metal Oxide Chemistry and Synthesis*; John Wiley & Sons: West Sussex, **2000**; pp 25– 137; Translated by E. Bescher.
8. Baes, C. G.; Mesmer, R. E. *The Hydrolysis of Cations*; John Wiley & Sons: New York, **1976**.
9. Liu, X.; Millero, F. J. The Solubility of Iron Hydroxide in Sodium Chloride Solutions *Geochim. Cosmochim. Acta* **1999**, 63, 3487– 3497 DOI: 10.1016/S0016-7037(99)00270-7
10. Zhu, M.; Frandsen, C.; Wallace, A. F.; Legg, B.; Khalid, S.; Zhang, H.; Mørup, S.; Banfield, J. F.;Waychunas, G. A. Precipitation pathways for ferrihydrite formation in acidic solutions *Geochim. Cosmochim. Acta* **2016**, 172, 247– 264 DOI: 10.1016/j.gca.2015.09.015
11. Cornell, R. M.; Schwertmann, U. *The Iron Oxides: Structure, Properties, Reactions, Occurrences and Uses*,2nd ed.; Wiley-VCH: Weinheim, **2003**.
12. Navrotsky, A.Size-Driven Structural and Thermodynamic Complexity in Iron Oxides *Science* **2008**,319, 1635– 1638 DOI: 10.1126/science.1148614
13. Baumgartner, J.; Dey, A.; Bomans, P. H. H.; Le Coadou, C. L.; Fratzl, P.; Sommerdijk, N. A. J. M.; Faivre, D.Nucleation and Growth of Magnetite from Solution *Nat. Mater.* **2013**, 12, 310– 314 DOI: 10.1038/nmat3558
14. Penn, R. L. Kinetics of Oriented Aggregation *J. Phys. Chem. B* **2004**, 108, 12707– 12712 DOI: 10.1021/jp036490+
15. Li, D.; Nielsen, M. H.; Lee, J. R. I.; Frandsen, C.; Banfield, J. F.; De Yoreo, J. J. Direction-Specific Interactions Control Crystal Growth by Oriented Attachment *Science* **2012**, 336, 1014– 1018 DOI: 10.1126/science.1219643
16. Mazeina, L.; Deore, S.; Navrotsky, A. Energetics of Bulk and Nano-Akaganeite, β-FeOOH: Enthalpy of Formation, Surface Enthalpy, and Enthalpy of Water Adsorption *Chem. Mater.* **2006**, 18, 1830– 1838 DOI: 10.1021/cm052543j
17. Fang, X.; Li, Y.; Chen, C.; Kuang, Q.; Gao, X.; Xie, Z.; Xie, S.; Huang, R.; Zheng, L. pH-Induced Simultaneous Synthesis and Self-Assembly of 3D Layered β-FeOOH Nanorods *Langmuir* **2010**, 26, 2745–2750 DOI: 10.1021/la902765p

18. Sugimoto, T.; Muramatsu, A. Formation Mechanism of Monodispersed a-Fe_2O_3 Particles in Dilute $FeCl_3$Solutions *J. Colloid Interface Sci.* **1996**, 184, 626– 638 DOI: 10.1006/jcis.1996.0660
19. Almeida, T. P.; Fay, M. W.; Zhu, Y.; Brown, P. D. Hydrothermal Growth Mechanism of α-Fe_2O_3 Nanorods Derived by Near In Situ Analysis *Nanoscale* **2010**, 2, 2390– 2399 DOI: 10.1039/c0nr00280a
20. Holm, N. G.; Dowler, M. J.; Wadsten, T.; Arrhenius, G. β-FeOOH•Cl_n (Akaganeite) and $Fe_{1-x}O$ (Wustite) in Hot Brine from the Atlantis II Deep (Red Sea) and the Uptake of Amino Acids by Synthetic β-FeOOH•Cl_n*Geochim. Cosmochim. Acta* **1983**, 47, 1465– 1470 DOI: 10.1016/0016-7037(83)90305-8
21. Yue, J.; Jiang, X.; Yu, A. Experimental and Theoretical Study on the β–FeOOH Nanorods: Growth and Conversion *J. Nanopart. Res.* **2011**, 13, 3961– 3974 DOI: 10.1007/s11051-011-0320-4
22. Atkinson, R. J.; Posner, A. M.; Quirk, J. P. Crystal Nucleation and Growth in Hydrolyzing Iron(III) Chloride Solutions *Clays Clay Miner.* **1977**, 25, 49– 56 DOI: 10.1346/CCMN.1977.0250108
23. Martell, A. E.; Smith, R. M.; Motekaitis, R. J. NIST critically selected stability constants of metal complexes database; NIST standard reference database 46.6.0, **2001**.
24. Fouilloux, S.SAXS Exploration of the Synthesis of Ultra Monodisperse Silica Nanoparticles and Quantitative Nucleation Growth Modeling *J. Colloid Interface Sci.* **2010**, 346, 79– 86 DOI: 10.1016/j.jcis.2010.02.052
25. Green, D. L.Size, Volume Fraction, and Nucleation of Stober Silica Nanoparticles *J. Colloid Interface Sci.* **2003**, 266, 346– 358 DOI: 10.1016/S0021-9797(03)00610-6
26. Abecassis, B.; Testard, F.; Spalla, O.; Barboux, P. *Nano Lett.* **2007**, 7, 1723– 1727 DOI: 10.1021/nl0707149
27. Polte, J.Nucleation and Growth of Gold Nanoparticles Studied via in situ Small Angle X-ray Scattering at Millisecond Time Resolution *ACS Nano* **2010**, 4, 1076– 1082 DOI: 10.1021/nn901499c
28. Viswanatha, R.Growth of Semiconducting Nanocrystals of CdS and ZnS *J. Nanosci. Nanotechnol.***2007**, 7, 1726– 1729 DOI: 10.1166/jnn.2007.706
29. Cravillon, J.; Schröder, C. A.; Nayuk, R.; Gummel, J.; Huber, K.; Wiebcke, M. Fast Nucleation and Growth of ZIF-8 Nanocrystals Monitored by Time-Resolved In Situ Small-Angle and Wide-Angle X-Ray Scattering*Angew. Chem.* **2011**, 123, 8217– 8221 DOI: 10.1002/ange.201102071
30. Ahmed, I. A. M.; Benning, L. G.; Kakonyi, G.; Sumoondur, A. D.; Terrill, N. J.; Shaw, S. J. Formation of Green Rust Sulfate: A Combined in Situ Time-Resolved X-ray Scattering and Electrochemical Study*Langmuir* **2010**, 26, 6593– 6603 DOI: 10.1021/la903935j
31. Jun, Y. S.; Lee, B.; Waychunas, G. A. In Situ Observations of Nanoparticle Early Development Kinetics at Mineral–Water Interfaces *Environ. Sci. Technol.* **2010**, 44, 8182– 8189 DOI: 10.1021/es101491e
32. Vehkamäki, H. *Classical Nucleation Theory in Multicomponent Systems*; Springer Verlag: Berlin, **2006**; pp42– 64.
33. IUPAC *Manual Of Symbols and Terminology for Physicochemical Quantities and Units. Appendix II: Definitions, Terminology and Symbols in Colloid and Surface Chemistry*; IUPAC: London, **1971**.
34. Einstein, A. *Investigations on the Theory of Brownian Movement*; Dover: New York, **1956**.
35. Blander, M.; Katz, J. L. The Thermodynamics of Cluster Formation in Nucleation Theory *J. Stat. Phys.* **1972**,4, 55– 59 DOI: 10.1007/BF01008471
36. Hexemer, A.; Bras, W.; Glossinger, J.; Schaible, E.; Gann, E.; Kirian, R.; MacDowell, A.; Church, M.;Rude, B.; Padmore, H. A SAXS/WAXS/GISAXS Beamline with Multilayer Monochromator *Journal of Physics: Conference Series* **2010**, 247, 012007 DOI: 10.1088/1742-6596/247/1/012007
37. Ilavsky, J.; Jemian, P. R. Irena: Tool Suite for Modeling and Analysis of Small-Angle Scattering *J. Appl. Crystallogr.* **2009**, 42, 347– 353 DOI: 10.1107/S0021889809002222
38. Feigin, L. A.; Svergun, D. I.; Taylor, G. W. *Structure Analysis by Small-Angle X-Ray and Neutron Scattering*;Plenum Press: New York and London, **1987**; pp 65– 72.
39. Porod, G. In *Small Angle X-Ray Scattering*, Glatter, O.; Kratky, O., Eds.; Academic Press: London, **1982**; pp18– 59.
40. Cai, J.; Liu, J.; Gao, Z.; Navrotsky, A.; Suib, S. L. Synthesis and Anion Exchange of Tunnel Structure Akaganeite *Chem. Mater.* **2001**, 13, 4595– 4602 DOI: 10.1021/cm010310w
41. Schwertmann, U. Solubility and Dissolution of Iron Oxides *Plant Soil* **1991**, 130, 1– 25 DOI: 10.1007/BF00011851

42. Jiang, J. Q.; Graham, N. J. D. Observations of the Comparative Hydrolysis/Precipitation Behaviour of Polyferric Sulphate and Ferric Sulphate *Water Res.* **1998**, 32, 930– 935 DOI: 10.1016/S0043-1354(97)83364-7
43. MacKay, A. L. Beta-ferric oxyhydroxide *Mineral. Mag.* **1960**, 32, 545– 557 DOI: 10.1180/minmag.1960.032.250.04
44. Asenath-Smith, E.; Estroff, L. A. Role of Akaganeite (β-FeOOH) in the Growth of Hematite (α-Fe_2O_3) in an Inorganic Silica Hydrogel *Cryst. Growth Des.* **2015**, 15, 3388– 3398 DOI: 10.1021/acs.cgd.5b00475
45. Grosse, A. A. V. The Relationship Between Surface Tension and Energy of Liquid Metals and Their Heat of Vaporization at the Melting Point *J. Inorg. Nucl. Chem.* **1964**, 26, 1349– 1361 DOI: 10.1016/0022-1902(64)80114-7
46. Casey, W. H.; Swaddle, T. W. Why Small? The Use of Small Inorganic Clusters to Understand Mineral Surface and Dissolution Reactions in Geochemistry *Rev. Geophys.* **2003**, 41, 1008 DOI: 10.1029/2002RG000118
47. Casey, W. H.; Rustad, J. R. Reaction Dynamics, Molecular Clusters, and Aqueous Geochemistry *Annu. Rev. Earth Planet. Sci.* **2007**, 35, 21– 46 DOI: 10.1146/annurev.earth.35.031306.140117
48. Zhu, M.; Legg, B. A.; Zhang, H.; Gilbert, B.; Ren, T.; Banfield, J. F.; Waychunas, G. A. Early Stage Formation of Iron Oxyhydroxides During Neutralization of Simulated Acid Mine Drainage Solutions *Environ. Sci. Technol.* **2014**, 46, 8140– 8147 DOI: 10.1021/es301268g
49. Panasci, A. F.; Ohlin, C. A.; Harley, S. J.; Casey, W. H. Rates of Water Exchange on the $[Fe_4(OH)_2(hpdta)_2(H_2O)_4]^0$ Molecule and Its Implications for Geochemistry *Inorg. Chem.* **2012**, 51, 6731–6738 DOI: 10.1021/ic300370q
50. Kanungo, S. B. Adsorption of Cations on Hydrous Oxides of Iron: I. Interfacial Behavior of Amorphous FeOOH and β-FeOOH (Akaganeite) in Different Electrolyte Solutions *J. Colloid Interface Sci.* **1994**, 162, 86–92 DOI: 10.1006/jcis.1994.1012
51. Kozin, P. A.; Boily, J. F. Proton Binding and Ion Exchange at the Akaganéite Interface *J. Phys. Chem. C***2013**, 117, 6409– 6419 DOI: 10.1021/jp3101046